

Accelerating the Lithium Storage Kinetics of Organosulfur Copolymers with Pyridine/Selenium Dual-Doping for Lithium-Organosulfur Battery

Wen-Wu Liu,* Hua-Xin Shen, Bo Lv, Ya-Wen Zheng, and Rong Zou*

Lithium-organosulfur batteries have positioned themselves at the forefront of energy storage due to high theoretical specific capacity, solid-solid reaction mechanism. In order to further decrease the shuttle effect and improve reaction kinetics, a copolymer cathode (PTSC) with short-chain sulfur ($R-S_4-R$) is first synthesized using propylene coordinated with carbon nanotube (CNT). Subsequently, pyridine and selenium atoms with well electroconductivity are introduced to synthesize the copolymer cathode (PTDSC, PTDSSeC). The lone pair electrons on nitrogen atoms within pyridyl groups establish strong Lewis acid-base interactions with lithium polysulfides, effectively anchoring active species and mitigating capacity fade; concurrently, the conjugated structure of pyridine rings optimizes electron transfer pathways

to enhance reaction kinetics. Selenium, leveraging its lower electronegativity, redistributes charge density to reduce S–S bond dissociation energy, facilitating reversible polysulfide conversion. The CNTs provide a 3D conductive scaffold and spatially confine polysulfides within the cathode. This synergy achieves quick kinetics of lithium polysulfides redox. Electrochemical result confirms that the copolymer cathode exhibits superior rate stability and capacity retention. Specifically, the PTDSSeC cathode maintains 76.4% of its reversible specific capacity after 500 cycles at a current density of 0.5 A g^{-1} . This work demonstrates the synergistic optimization of “low shuttle-high activity-fast conduction” through the integration of short-chain sulfur, pyridine functional groups, and selenium atoms.

1. Introduction

With the global shift toward low-carbon energy structures, high-energy-density energy storage technology has emerged as a core driving force for advancing electric vehicles, smart grids, and portable electronic devices.^[1–3] Lithium–sulfur (Li–S) batteries, exhibiting significant advantages including high theoretical energy density (2600 Wh kg^{-1}), theoretical specific capacity (1675 mAh g^{-1}), abundant sulfur resources, low cost, and environmental friendliness, are regarded as one of the most promising next-generation energy storage systems.^[4–6] Compared with traditional lithium-ion batteries (LIBs), the combination of sulfur cathode and lithium metal anode in Li–S batteries overcomes the capacity bottleneck of transition metal oxide cathodes, achieving a theoretical energy density exceeding eight times that of commercial LIBs.^[7–9] This provides a crucial technological pathway for addressing “range anxiety” and “cost pressure” in the energy storage domain.

The practical deployment of Li–S batteries remains impeded by multiple intrinsic challenges. The core limitations arise from the properties of the sulfur cathode and electrolyte: elemental sulfur and its discharge product Li_2S exhibit poor electronic conductivity ($<10^{-3} \text{ S cm}^{-1}$), falling below the minimum threshold required for effective electrode operation ($<10^{-3} \text{ S cm}^{-1}$), which results in sluggish reaction kinetics;^[10] polysulfides (LiPSs) demonstrate high solubility in ether-based electrolytes, enabling soluble species ($\text{Li}_{2-x}\text{S}_x$, $4 \leq x \leq 8$) to migrate across the separator toward the anode under concentration gradients, where reduction to lower sulfides occurs without complete reversion to the cathode, a phenomenon termed the “shuttle effect”,^[11] causing active material loss, reduced Coulombic efficiency, and lithium anode corrosion; the sulfur cathode undergoes 80% volume variation during cycling, inducing electrode structural degradation. Additionally, lithium metal anodes are prone to dendritic growth that risks internal short circuits through separator penetration, while unstable solid–electrolyte interphase (SEI) formation exacerbates capacity fade.^[12,13] Collectively, these issues constrain cycle stability and rate capability, thus leading to major commercialization barriers. Simultaneously, traditional LIBs achieve practical capacities reaching 90% of their theoretical capacity; Li–S batteries typically deliver practical capacities below 70% of the theoretical value.^[14]

To address the numerous challenges encountered by lithium–sulfur battery cathodes during charge–discharge cycles, scientists have explored multiple strategies; carbon materials emerge as the preferred sulfur hosts due to their high electrical conductivity, tunable pore structures, and chemical stability, exemplified by

W.-W. Liu, H.-X. Shen, B. Lv, Y.-W. Zheng, R. Zou
State Key Laboratory of Advanced Processing and Recycling of Nonferrous Metals
Lanzhou University of Technology
Lanzhou 730050, PR China
E-mail: wvliu@lut.edu.cn
zourong18394024456@163.com

W.-W. Liu, H.-X. Shen, B. Lv, Y.-W. Zheng, R. Zou
College of Materials Science and Engineering
Lanzhou University of Technology
Lanzhou 730050, PR China

 Supporting information for this article is available on the WWW under <https://doi.org/10.1002/batt.202500741>

conductive carbon,^[15] carbon nanotubes (CNTs),^[16] and graphene.^[17] Sulfur–carbon composite materials, by confining sulfur within carbon matrices, simultaneously resolve poor electrical conductivity and volume expansion issues while inhibiting polysulfide shuttling through physical adsorption.^[18] Early researchers implemented physical modifications, such as He et al.^[19] confined sulfur in materials with porous carbon matrix, the pore structure of porous carbon provides storage space for sulfur. Nevertheless, the weak interaction between nonpolar carbon and polar polysulfides, the inherent shuttle effect cannot be fully resolved.^[20] Consequently, scientists have initiated the introduction of organic or inorganic metal-based materials as carriers with functional optimization, resulting in the emergence of various composite materials, including metal atoms,^[21] metal phosphides,^[22] nitrides,^[23] sulfides,^[24] metal–organic frameworks,^[25] and single-atom catalysts compounded with carbon materials.^[26] Zhang et al.^[27] prepared a 3D graphene nanosheet–carbon nanotube (GN-CNT) matrix via a one-pot pyrolysis process and added cobalt nanoparticles with different diameters into the matrix. These composite enhances the charge transfer and electrolyte wettability of the cathode materials simultaneously, the addition of cobalt nanoparticles greatly promotes the mutual conversion between high-order and low-order polysulfides. These materials significantly enhance battery performance through dual mechanisms: on the one hand, by forming strong chemisorption with polysulfides via active surface sites,^[28,29] on the other hand, by employing catalytic activity to reduce the energy barrier of sulfur conversion reactions, accelerating multistep reaction kinetics.^[30,31] Despite substantial achievements in sulfur cathode catalysis for Li–S batteries, the unavoidable solid–liquid–solid phase transition issues during the conversion from long-chain to short-chain sulfur persist, lithium polysulfides (LiPSs) cannot be fundamentally eliminated, and the shuttle effect remains difficult to resolve.

Organic sulfur polymers, as a highly promising class of cathode materials, have gained widespread attention in recent years due to their abundant resources, excellent environmental compatibility, and strong structural designability.^[32] Unlike the octatomic ring structure of conventional sulfur cathodes, sulfur atoms in polymer materials are predominantly bonded as sulfur chains via strong covalent C–S bonds to the organic carbon chain backbone, forming a unique $-C-S_n-C-$ structure, wherein the sulfur chains serve as the primary active component,^[33,34] while the carbon chains function as an inactive support scaffold. Sulfur chain length serves as a critical parameter for regulating electrochemical performance: shortening sulfur chains significantly reduces the generation of soluble higher-order LiPSs. Designing organic sulfur cathodes with short sulfur chains transforms the reaction mechanism from the conventional “solid–liquid–solid” conversion to a “solid–solid” reaction during charge/discharge, fundamentally suppressing the shuttle effect.^[35] However, short sulfur chain design inevitably reduces theoretical capacity.^[36–38] Therefore, sulfur chain regulation must balance sulfur content to reconcile capacity and stability. Modifying functional groups in carbon chains to construct uniform electron/ion conduction networks, optimize interactions with LiPSs, and enhance charge

transfer kinetics is essential for improving the uniformity of electrochemical reactions in sulfur chain segments.^[39–41] For instance, aromatic groups or heteroatoms can further enhance conductivity and electrochemical performance. At the molecular level, precise regulation of redox pathways can be achieved by controlling sulfur chain length and carbon chain structure (functional group modification, monomer selection), leveraging the strong chemical interactions between organic components and sulfur to optimize electrochemical performance. Our group^[42] synthesized an organic sulfur polymer containing short-chain sulfur (P4SSe) via interfacial polymerization, effectively improving the Marcus electron transfer rate of the cathode, and elucidated the redox mechanism through density functional theory calculations. However, although controllable molecular structures offer commercialization prospects, challenges such as the high bond dissociation energy of S–S bonds, poor electrical conductivity, and sluggish redox kinetics still require further research for resolution.

In this work, an organic sulfur copolymer cathode (PTSC) with short sulfur chains (R-S4-R) was synthesized through molecular engineering design and interface regulation, utilizing propyl groups as the carbon backbone in conjunction with crosslinked random CNTs. Furthermore, pyridine was introduced as a functional group to copolymerize with propyl groups, synthesizing another organic sulfur copolymer cathode (PTDSC). Due to the sulfur atoms existing in the form of S–S–S–S tetrasulfide short chains, the constant-current charge–discharge curves of the polymer cathodes exhibited a solid–solid single plateau, without the double-plateau curve characteristic of conventional sulfur cathode. The charge–discharge mechanism of the organic sulfur polymer cathode was analyzed based on measured cyclic voltammetry (CV) curves combined with constant-current charge–discharge profiles. To further enhance the redox kinetics during cycling, promoting faster conversion of the sulfur copolymer cathode, selenium atoms were covalently bonded into the pyridine-containing propyl backbone (R-SeS₃-R), constructing a hierarchical organic sulfur/carbon nanotube composite cathode (PTDSSeC). The strategic implementation of short sulfur chains effectively suppresses the shuttle effect through a solid–solid conversion mechanism. Concurrently, pyridyl groups anchor active substances and optimize electron transport pathways, while selenium doping enhances copolymer conductivity and facilitates reversible polysulfide conversion. Furthermore, the integrated CNT framework establishes rapid electron conduction channels for the short-chain sulfur species. As a result, this cathode delivered a specific capacity of 706.4 mAh g⁻¹ at 0.5 A g⁻¹ and maintained 76.4% capacity retention after 500 long-term cycles at this current density.

2. Results and Discussion

The fabrication process of the organic sulfur/carbon nanotube composite cathode is illustrated in Figure 1a. The sodium polysulfide precursor was first prepared, and the Na₂S solution was prepared by dissolving sodium sulfide nonahydrate (Na₂S·9H₂O) in deionized water under an argon atmosphere with stirring.

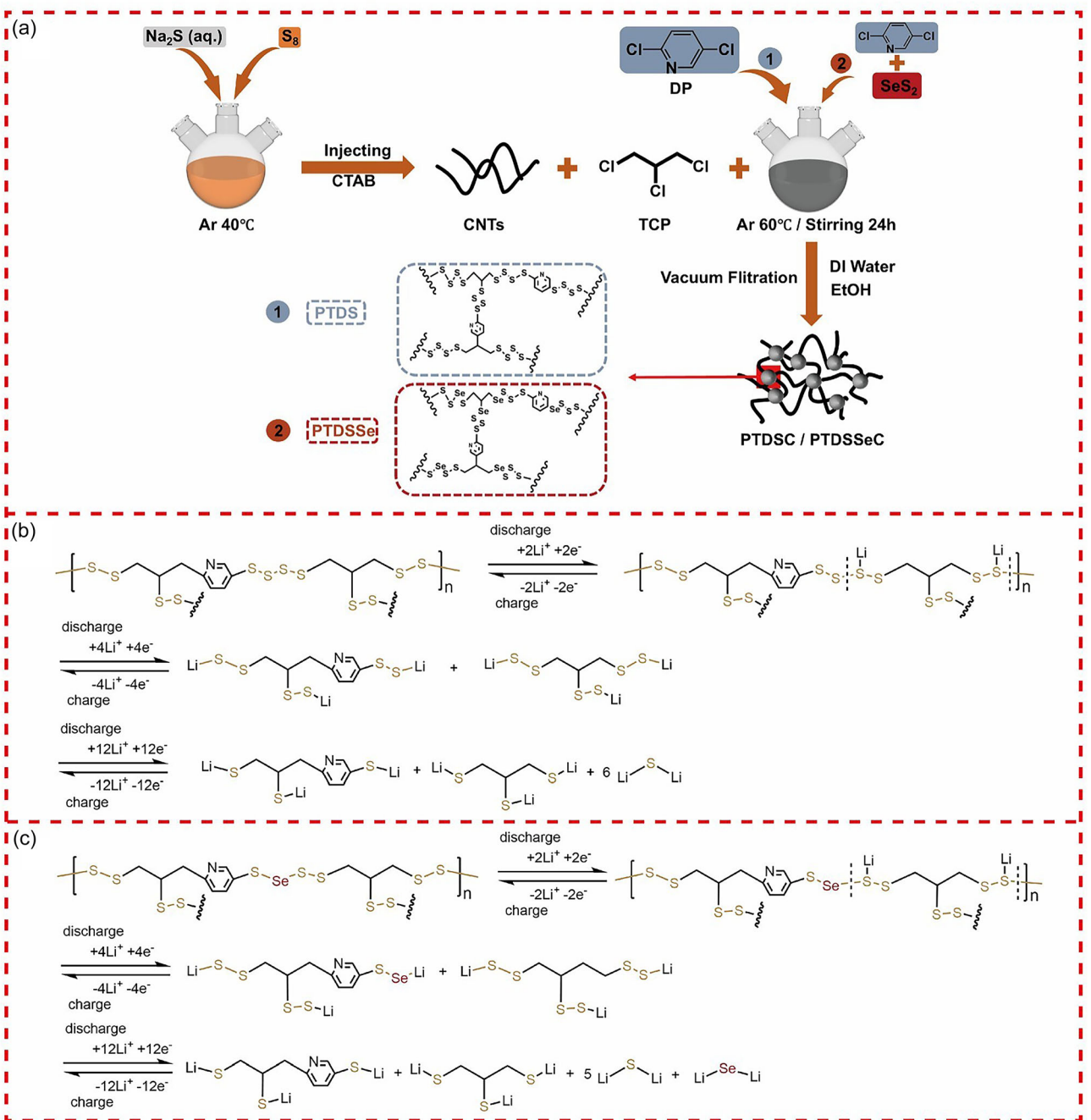


Figure 1. a) Schematic representation of the synthesis process for the organosulfur copolymer cathode (PTDSC) and the selenium-doped organosulfur copolymer cathode (PTDSSeC). b,c) Proposed discharge/charge mechanism of PTDSC and PTDSSeC cathodes.

The Na_2S solution was subsequently mixed with sulfur powder at a molar ratio of 1:3 to prepare a Na_2S_4 solution for precise control of the sulfur chain length ($-\text{S}-\text{S}-\text{S}-$) covalently bonded to the propyl group. The prepared sodium polysulfide precursor solution and 1,2,3-trichloropropane (TCP) were injected into a hexadecyltrimethylammonium bromide (CTAB) aqueous solution under an argon atmosphere. The reaction mixture was heated in an oil bath with stirring for 24 h, and a cream-colored suspension was ultimately obtained. In this process, cetyltrimethylammonium bromide (CTAB), as a cationic surfactant, formed a micellar

structure through its long-chain alkyl group and hydrophilic quaternary ammonium group in the reaction system, providing microenvironmental catalytic sites for the condensation polymerization between the sulfur chain ($-\text{S}-\text{S}-\text{S}-$) in the precursor and 1,2,3-trichloropropane (TCP). The quaternary ammonium cation (N^+) of CTAB activates the nucleophilic sites (S^{2-}) of the sulfur chain via electrostatic interactions, while weakening the polarity of the C—Cl bonds in TCP, promoting the nucleophilic substitution reaction (sulfur atoms attacking the saturated carbon atoms of TCP) to form strong C—S bonds, thereby achieving covalent

bonding of short sulfur chains to the carbon skeleton. After the reaction, the suspension was collected as the organic sulfur polymer particles via vacuum filtration through filter paper, with a large amount of deionized water and anhydrous ethanol used during this process to remove byproducts; after collection, the product was dried in a vacuum oven to obtain the final product.

As shown in Figure S1, Supporting Information, we illustrate the pristine organic sulfur polymer (PTS) without incorporated heteroatoms, CNTs, or other active functional groups as a baseline; the two polymers displayed in the figure consist of the organic sulfur polymer additionally doped with 2,5-dichloropyridine (DP), designated as PTDS, and the organic sulfur polymer further doped with selenium atoms, denoted as PTDSSe. Accordingly, the polymers formed by additional doping of CNTs into PTDS and PTDSSe are designated as PTDSC and PTDSSeC, respectively. Figure S1a, Supporting Information, shows light yellow particles of PTS (Supporting Information); to achieve a more uniform dispersion of the organic sulfur polymer within the CNTs network, CNTs were added during the interfacial polycondensation process, yielding the black powder-form organic sulfur polymer (PTSC) in Figure S1b, Supporting Information. Based on electrochemical performance tests, the charge-discharge reaction mechanisms of organic sulfur polymers were elucidated. Figure 1b, c and S2, Supporting Information, illustrate the redox reaction mechanisms during charge-discharge processes for PTDSC, PTDSSeC, and PTSC, respectively. During

discharge, lithium ions initially bind to sulfur or selenium atoms in tetrasulfide ($-S_4-$) or selenotrisulfide ($-S_3Se-$) moieties upon electron transfer. This corresponds to the first reduction peak at 2.25–2.33 V in CV curves and the sloping region in galvanostatic charge-discharge (GCD) profiles. Subsequently, cleavage of S—S and S—Se bonds generates unstable intermediates that undergo further reduction to form fully discharged organic sulfides/selenides, accompanied by Li_2S/Li_2Se precipitation, aligning with the subsequent two reduction peaks in CV curves and the discharge plateau in GCD curves. To further analyze the morphology and elemental distribution of organic sulfur polymer cathodes, three types of organic sulfur polymer materials were subjected to scanning electron microscopy (SEM) and energy-dispersive spectroscopy (EDS) tests.

Figure 2a–c shows the SEM images of the PTSC, PTDSC, and PTDSSeC cathode at different magnifications, respectively. It can be visually observed that the organic sulfur polymer cathode is dispersed as nanospheres throughout the interconnected CNT networks. This spherical polymer morphology, coupled with the reticulated CNT architecture, ensures sufficient electrolyte wettability while effectively mitigating the inherently poor conductivity of organic sulfur polymers.^[43] Afterwards, Figure 2j–n displays the EDS mapping of the PTDSSeC cathode, where sulfur and selenium exhibit spherical profiles of elemental distributions, confirming their presence within the organic sulfur polymer cathode. Combined with the uniform carbon elemental distribution,

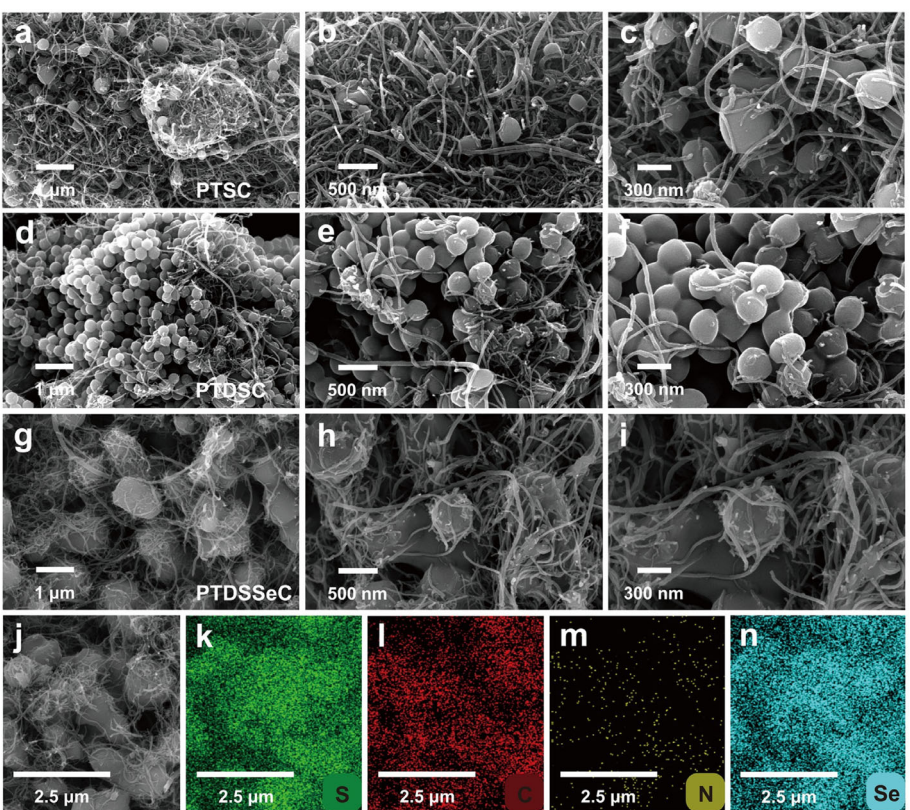


Figure 2. SEM images of a–c) PTSC, d–f) PTDSC, and g–i) PTDSSeC cathode under different magnifications. j–n) EDS images of sulfur, carbon, nitrogen, and selenium elements on PTDSSeC cathode.

this result further corroborates the even distribution of sulfur and selenium elements in organic polymer. Besides, Figure S3 and S4, Supporting Information, display the SEM and EDS images of PTSC and PTDSC cathode (Supporting Information), respectively. Owing to the absence of pyridine doping in PTSC, its EDS map shows no nitrogen elemental distribution. The SEM images reveal similar spherical morphologies for both organic sulfur polymer cathodes and the PTDSSeC cathode.

To demonstrate the successful synthesis of organic sulfur polymers, multiple analytical techniques are employed to characterize the physicochemical properties of the prepared samples. As illustrated in Figure 3a, it can be observed from the X-ray diffraction patterns that differing from the distinct characteristic diffraction peaks possessed by selenium disulfide (SeS_2), 2,5-dichloropyridine (DP), and sulfur, PTSC, PTDSC, and PTDSSeC all exhibit amorphous broad peaks, showing no obvious visible crystalline domains. The low-intensity amorphous peaks in the $15^\circ\text{--}40^\circ$ range corresponding to the characteristic diffraction peaks of selenium disulfide and sulfur indicate that the two

substances are successfully transformed into amorphous polysulfur (selenium) chains within the propyl framework, thereby proving the successful synthesis of organic sulfur polymers through polycondensation reaction. As shown in Figure 3b, PTSC, PTDSC, and PTDSSeC in the vicinity of 30° exhibit characteristic peaks partially overlapping with diffraction peak of CNTs; this range corresponds to the characteristic peak of graphite (002) crystal face,^[44] indicating the successful loading of organosulfur polymers onto CNTs. Raman spectroscopy is further carried out to investigate the chemical structures of organic sulfur polymers, as shown in Figure 3c, for the purpose of excluding the interference of intense carbon signal peaks produced by CNTs during Raman measurements with the signals of other bonds (S—Se, S—S, C—S), three organic sulfur polymer cathodes without doped CNTs are selected to availablely analyze. Among them, three polymer cathodes all exhibit distinct S—S bond stretching vibrations at 490 cm^{-1} , corresponding to $3\text{S}(\text{—S—S—S—})$ and $4\text{S}(\text{—S—S—S—S—})$ bond of sulfur chain structures,^[45] which is consistent with previous existing research results. The peaks appearing at 700 cm^{-1} for

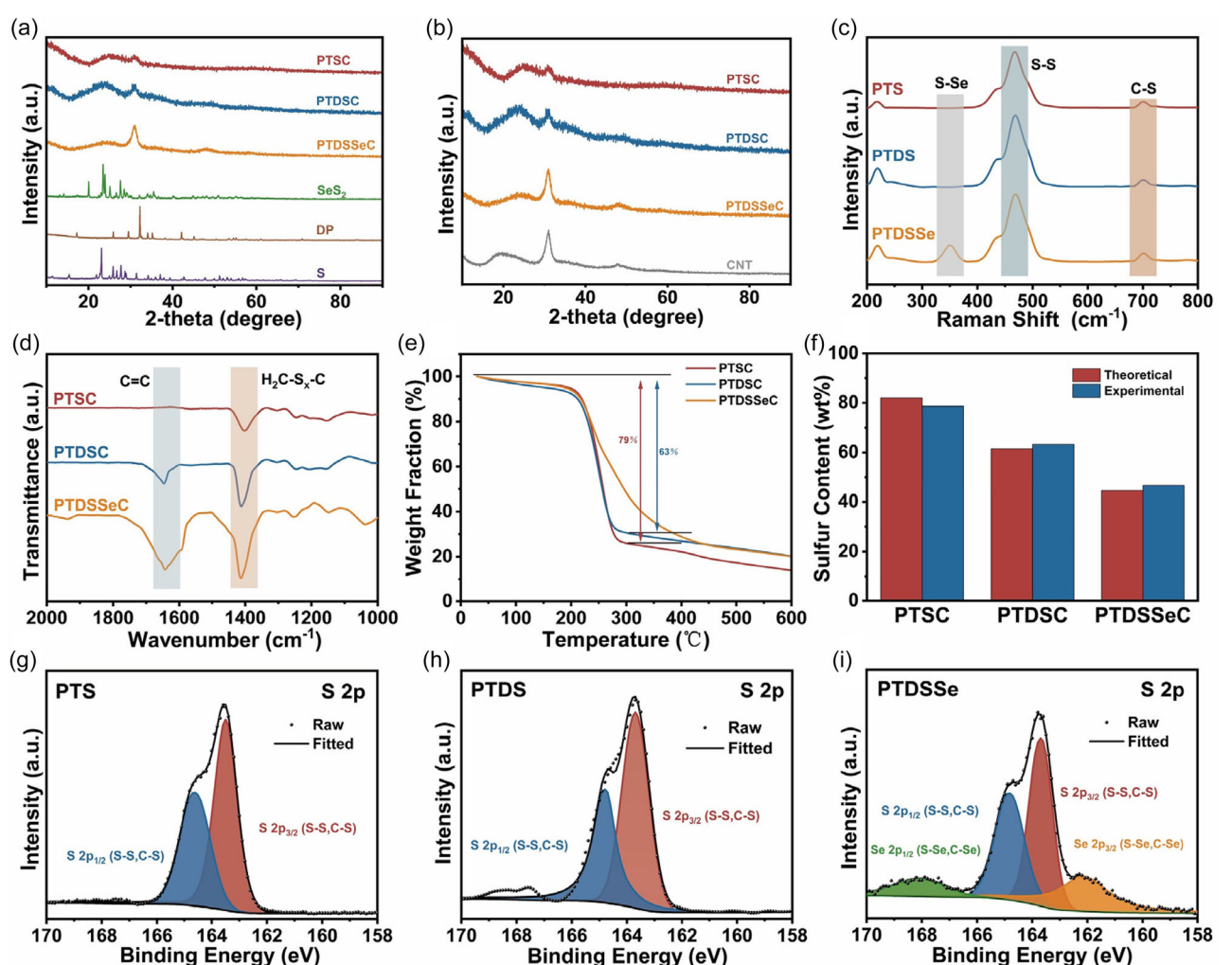


Figure 3. XRD patterns of a) PTSC, PTDSC, PTDSSeC, selenium disulfide (SeS_2), 2,5-dichloropyridine (DP), sulfur (S_8), and b) CNTs. c) Raman spectra of PTS, PTDS, and PTDSSe, respectively. d) FT-IR spectra and e,f) TGA curves and EA tests of PTSC, PTDSC, and PTDSSeC, respectively. g-i) XPS images of S 2p for PTS, PTDS, and PTDSSe, respectively.

the three polymers correspond to C—S bond stretching vibrations, proving that sulfur atoms are covalently bonded to the carbon skeleton.^[46,47] Furthermore, PTDSSe demonstrates a peak at 349 cm⁻¹, which is not possessed by PTS or PTDS, corresponding to S—Se bond vibrations,^[48] thus proving that selenium atoms are successfully bonded to the sulfur chain. Here, XPS (X-ray Photoelectron)spectroscopy further corroborates the above viewpoint. From the XPS full-spectra in Figure S5, Supporting Information, it can be intuitively seen that carbon, sulfur, and nitrogen elements simultaneously exist in the three polymers as well as PTDSSe and PTDS. Whereas, the reason for the weak N 1s characteristic peak signals in PTDS and PTDSSe is related to the small amount of pyridine group addition. Furthermore, Se 3d signals were detected in PTDSSe. In Figure 3g–i, the appearance of S 2p_{3/2} and S 2p_{1/2} characteristic peaks of three organic sulfur polymers is attributed to the existence of S—S bonds and C—S bonds, with an energy difference of 1.2 eV, demonstrating that the S atom exists in covalent bonding with C atom. Notably, PTDSSe exhibits characteristic peak signals at 168.0 and 162.1 eV corresponding to Se 3p_{1/2} and Se 3p_{3/2},^[49] and partially overlaps with the S 2p characteristic peaks. Consequently, combined with the detected Se 3d signals in the full spectrum, it is confirmed that covalent bonding is successfully formed between selenium and carbon/sulfur atoms in PTDSSe through interfacial polycondensation reaction.

Fourier transform infrared spectroscopy (FT-IR) (Figure 3d) further proves the structural connection of the three organic sulfur polymers. A characteristic double-bond signal at 1643 cm⁻¹, attributed to C=N stretching vibrations of the pyridyl group, was observed in both PTDSSeC and PTDSC composites, whereas this diagnostic peak was absent in PTSC (which lacks pyridine doping). A peak appears at 1400 cm⁻¹ representing the CH₂—S_x—C deformation vibration of PTSC, PTDSC, and PTDSSeC,^[50] proving that the sulfur chains are covalently bonded to the propyl carbon skeleton in the three polymers. Combined with the pyridine group stretching vibration peaks appearing at 1643 cm⁻¹ in PTDSSeC and PTDSC cathode, these results further explain that the pyridine groups are successfully introduced to these two substances. Thermogravimetric analysis (TGA) is utilized to verify the sulfur content of three polymers, as shown in Figure 3e, the plot of PTSC rapidly decreases by 79.0 wt% at the temperature range of 200–300 °C, that is, the sulfur content of PTSC reaches 79.0 wt%. Thermogravimetric curve of PTDSC rapidly decreases by 63.0 wt% at 200–300 °C temperature range, signaling that the sulfur content is about 63.0 wt%. Unlike the above two polymers, the thermogravimetric curve of PTDSSeC exhibits bimodal decomposition characteristics, wherein sulfur loses weight by 46.5 wt% in the range of 200–300 °C temperature, and selenium range loses weight by 15.5 wt% in the range of 200–300 °C temperature. The elemental content characterization of three organic sulfur polymers is conducted via the element analysis (EA) method, as shown in Figure 3f, sulfur elemental contents of PTSC, PTDSC, and PTDSSeC are 78.69, 63.23, and 46.53%, respectively, which are close to the theoretical sulfur content values and consistent with the thermogravimetric test results. Detailed elemental analysis result values are provided in Table S1, Supporting Information.

To evaluate the performance of PTSC, PTDSC, and PTDSSeC cathode materials, CR2032 coin batteries are assembled using three cathode materials and lithium metal anode, respectively, and the electrochemical performance tests are characterized in detail, respectively. Figure 4a,d displays the CV curves of the first three cycles for PTDSSeC cathode at 0.1 mV s⁻¹ scan rate and CV curves at 0.1–0.5 mV s⁻¹ scan rate, respectively. The CV curves of PTSC and PTDSC cathodes are also provided to investigate the redox characteristics of the three cathode materials, as illustrated in (Figure S6, Supporting Information). Obviously, three reduction peaks can be clearly observed from the CV curves of the three organic sulfur polymer cathodes, as shown in Figure 4a, the first reduction peak at 2.25–2.33 V corresponds to the first step lithiation process during discharge of sulfur atoms or selenium atoms from sulfur chains at tetrasulfide bonds (—S₄) or selenotrisulfide bonds (—S₃Se—). Subsequently, the lithiated intermediates eventually convert to fully discharged organic sulfur (selenium) compounds and Li₂S/Li₂Se in the two discharge stages at 2.14–2.24 V and 1.98–2.05 V.^[51,52] According to comparative observation of the CV curves of the three organic sulfur cathodes, it can be clearly seen that the PTDSSeC cathode has the highest oxidation and reduction peak currents. The aforementioned electrochemical analysis corroborates the redox reaction mechanism during charge–discharge processes depicted in Figure 1. Furthermore, the CV curves consistency of the first three cycles is better, and the PTDSSeC cathode has better shape retention at different scan rates, which proves that the organic sulfur cathode material doped with pyridine and selenium atoms has more excellent redox kinetics and electrochemical cycling reversibility. Figure 4b,c shows the Tafel curves of three organic sulfur cathodes at a scan rate of 0.1 mV s⁻¹. As shown in Figure 4b, the fitted Tafel slopes for the reduction process of PTSC, PTDSC, and PTDSSeC cathodes are 70.8, 60.4, and 33.7 mV dec⁻¹, respectively, while the fitted Tafel slopes for the oxidation process are 49.3, 43.4, and 32.9 mV dec⁻¹, respectively. Compared with the other two polymer cathodes, the PTDSSeC cathode possesses the lowest Tafel slope, a lower Tafel slope indicates stronger redox reaction kinetics. Next, the reaction kinetics of three organic sulfur polymer cathodes are further evaluated by using the Randles–Sevcik Formula (1), as shown below.^[53]

$$I_p = 26900n^{1.5} AD_{Li^+}^{0.5} v^{0.5} C_{Li^+} \quad (1)$$

where I_p is the peak current (A), n is the number of transferred electrons for the redox reaction, A is the area of the cathode sheet (cm²), D_{Li^+} is the lithium-ion diffusion coefficient (cm² s⁻¹), C_{Li^+} is the concentration of lithium-ion (mol cm⁻³), and v is the scan rate (V s⁻¹). From the above formula, it can be intuitively seen that the peak current exhibits a linear relationship with the square root of the scan rate. Therefore, the function relationship of the peak current as the vertical coordinate and the square root of the scan rate as the horizontal coordinate is conducted, then the magnitude of the fitted slope can be employed to evaluate the lithium-ion diffusion behavior. As shown in Figure 4e,f, the fitted slopes for the reduction process of PTSC, PTDSC, and PTDSSeC cathodes are -1.69, -2.31, and -4.28, respectively, while the fitted slopes

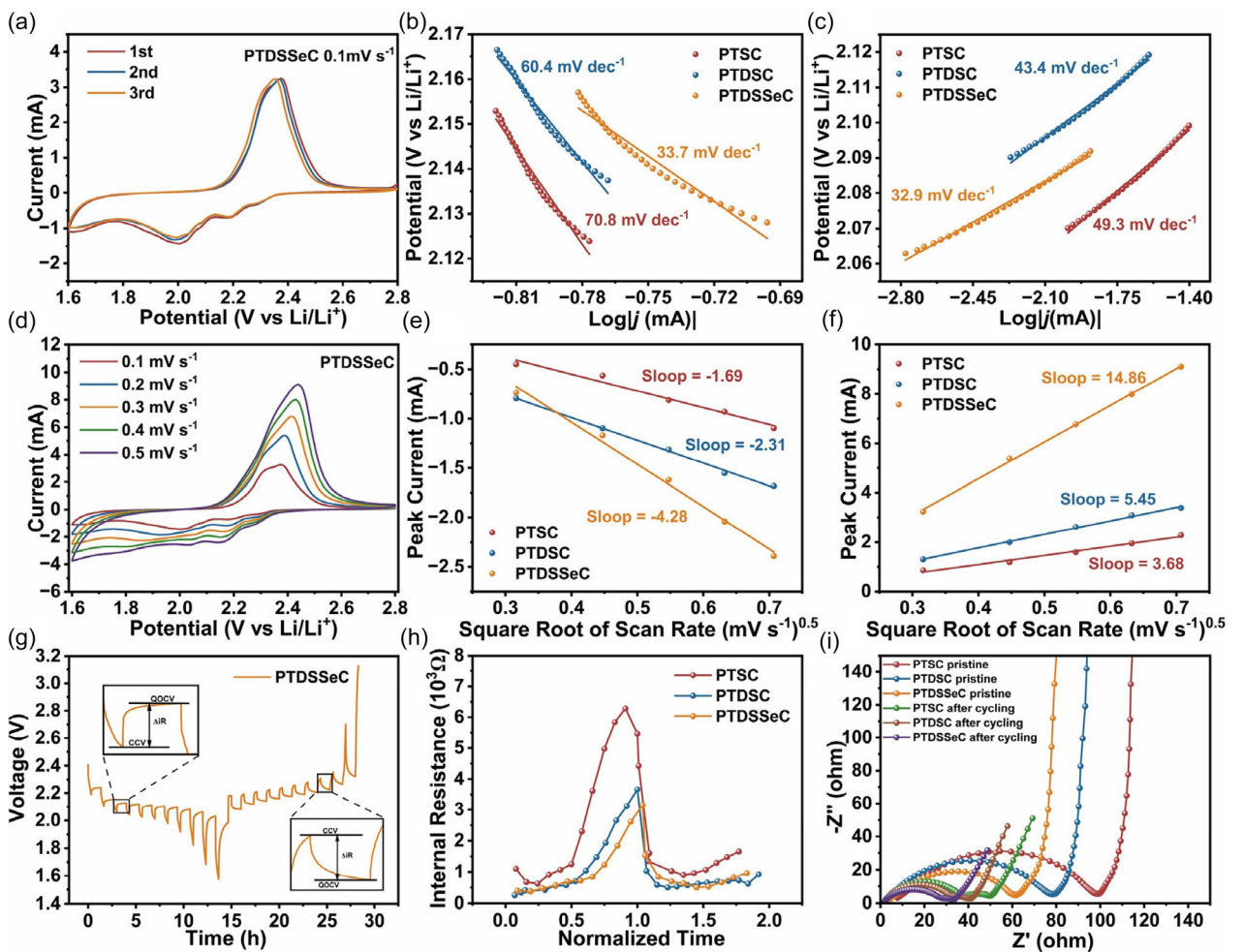


Figure 4. CV curves of PTDSSeC cathodes a,d) at scan rate of 0.1 mV s^{-1} for the initial three cycles and at scan rates of $0.1\text{--}0.5 \text{ mV s}^{-1}$, respectively. b,c) Tafel slope plots and e,f) peak currents of the CV versus the square root of the scan rate for the redox processes of PTSC, PTDSC, and PTDSSeC cathodes, respectively. g) GITT curves of PTDSSeC. h) Internal resistance of PTSC, PTDSC, and PTDSSeC. i) Nyquist plots of PTSC, PTDSC, and PTDSSeC cathodes before and after cycling, respectively.

for the oxidation process are 3.68, 5.15, and 14.86 mV s^{-1} , respectively. The absolute values of the redox fitted slopes of the PTDSSeC cathode are all higher than those of the other two organic sulfur polymer cathodes, which proves that the lithium-ion diffusion kinetics properties of the pyridine and selenium atom-doped PTDSSeC cathode material are the most excellent in these three cathodes. According to Formula (1), the D_{Li^+} (lithium-ion diffusion coefficient) of the three cathode materials can be calculated by inputting experimental parameters. Specifically, in the reduction process, the D_{Li^+} of PTSC, PTDSC, and PTDSSeC cathodes is 4.47×10^{-14} , 8.36×10^{-14} , and $2.86 \times 10^{-13} \text{ cm}^2 \text{ s}^{-1}$, respectively. While in the oxidation process, the D_{Li^+} of three organic sulfur polymer cathodes are 2.12×10^{-13} , 4.65×10^{-13} , and $3.45 \times 10^{-12} \text{ cm}^2 \text{ s}^{-1}$, respectively. As a consequence, the above results suggest that the PTDSSeC cathode has the best lithium-ion diffusion ability.

Moreover, the galvanostatic intermittent titration technique (GITT) analysis is performed on PTSC, PTDSC, and PTDSSeC cathodes at a current density of 0.1 A g^{-1} (Figure 4g), which is used to detect the internal resistance variation of the battery during charge

and discharge processes. Figure S7, Supporting Information, shows the GITT test curves for PTSC and PTDSC cathodes (Supporting Information). Simultaneously, the diffusion resistance ΔR can be theoretically calculated by Formula (2), where $\Delta V_{\text{QOCV}-\text{CCV}}$ is the potential difference between the quasi-open-circuit voltage and closed-circuit voltage, as shown in the local enlarged views of curves in Figure 4g and S7, Supporting Information, and I_{applied} is the current applied to the electrode.

$$\Delta R = \frac{|\Delta V_{\text{QOCV}-\text{CCV}}|}{I_{\text{applied}}} \quad (2)$$

According to the calculation results of Formula (2),^[54] the diffusion resistance curves of PTSC, PTDSC, and PTDSSeC cathodes are plotted, as shown in Figure 4h, it can be precisely seen that the increase in diffusion resistance of the PTDSSeC cathode is smaller. Therefore, the lower internal resistance is mainly attributed to that the conjugated structure of the pyridine ring substantially optimizes the electron transport pathway and enhances the reaction kinetics performance. Meanwhile, the selenium atom has higher

conductivity, further promoting efficient electron transport. Besides, the electrochemical impedance spectroscopy (EIS) tests are performed on PTSC, PTDSC, and PTDSSeC cathodes before and after cycling (Figure 4i), and an equivalent circuit model is applied to fit the EIS spectra (Figure S8, Supporting Information). The Nyquist plot curves of PTSC, PTDSC, and PTDSSeC cathodes all appear in semicircles in the medium–high frequency region, while in the low-frequency region, they appear a slanted lines, where the semicircle curve corresponds to the charge transfer resistance (R_{ct}), and the slanted line corresponds to the Warburg impedance (W_o).^[55] Before cycling, the PTDSSeC cathode has the lowest impedance, which is consistent with the above calculated diffusion resistance, further confirming that the pyridine groups and selenium atoms significantly enhance the conductivity of the polymer. In the Nyquist plot curves after cycling, a significant reduction in charge transfer impedance and a great enhancement in activation degree can be observed for all three cathode materials.^[56] It is not different to observe that a new semicircular region appears between the charge transfer resistance (R_{ct}) and Warburg impedance (W_o) before cycling, corresponding to the surface resistance (R_s). This semicircle is closely related to the irreversible Li₂S/Li₂Se deposition after electrode activation and the formation of the

solid–electrolyte interphase (CEI). Both before and after cycling, the PTDSSeC cathode exhibits the smallest R_{ct} and surface resistance (R_s). Consequently, these results fully confirm that the doping of pyridine groups and selenium atoms effectively improves the redox kinetics performance of the polymer cathode and promotes the lithiation process of the organic sulfur cathode during electrochemical reactions.

To further investigate the electrochemical performance of organic sulfur polymer cathode materials, Figure 5a demonstrates the rate performance test of three polymer cathodes, the current density is gradually increased from 0.1 A g⁻¹ to 0.5, 1, 2, 3 A g⁻¹, finally returning to 0.1 A g⁻¹. The specific capacities of the PTSC cathode are 423.5, 298.8, 242.9, 195.4, 175.3, and 342.2 mA h g⁻¹ at these current densities, while the specific capacities of the PTDSSeC cathode are 801.9, 670.6, 506.1, 438.8, 422.1, and 735.7 mA h g⁻¹, showing higher specific capacity and superior electrochemical stability and reversibility. Figure 5b presents the 100-cycle short-term cycling tests of three organic sulfur polymer cathodes at 0.1 A g⁻¹, where initial specific capacities of PTSC, PTDSC, and PTDSSeC were measured at 425.5, 662.9, and 805.9 mA h g⁻¹, respectively, retaining 231.3, 430.3, and 636.1 mA h g⁻¹ after 100 cycles, corresponding to capacity

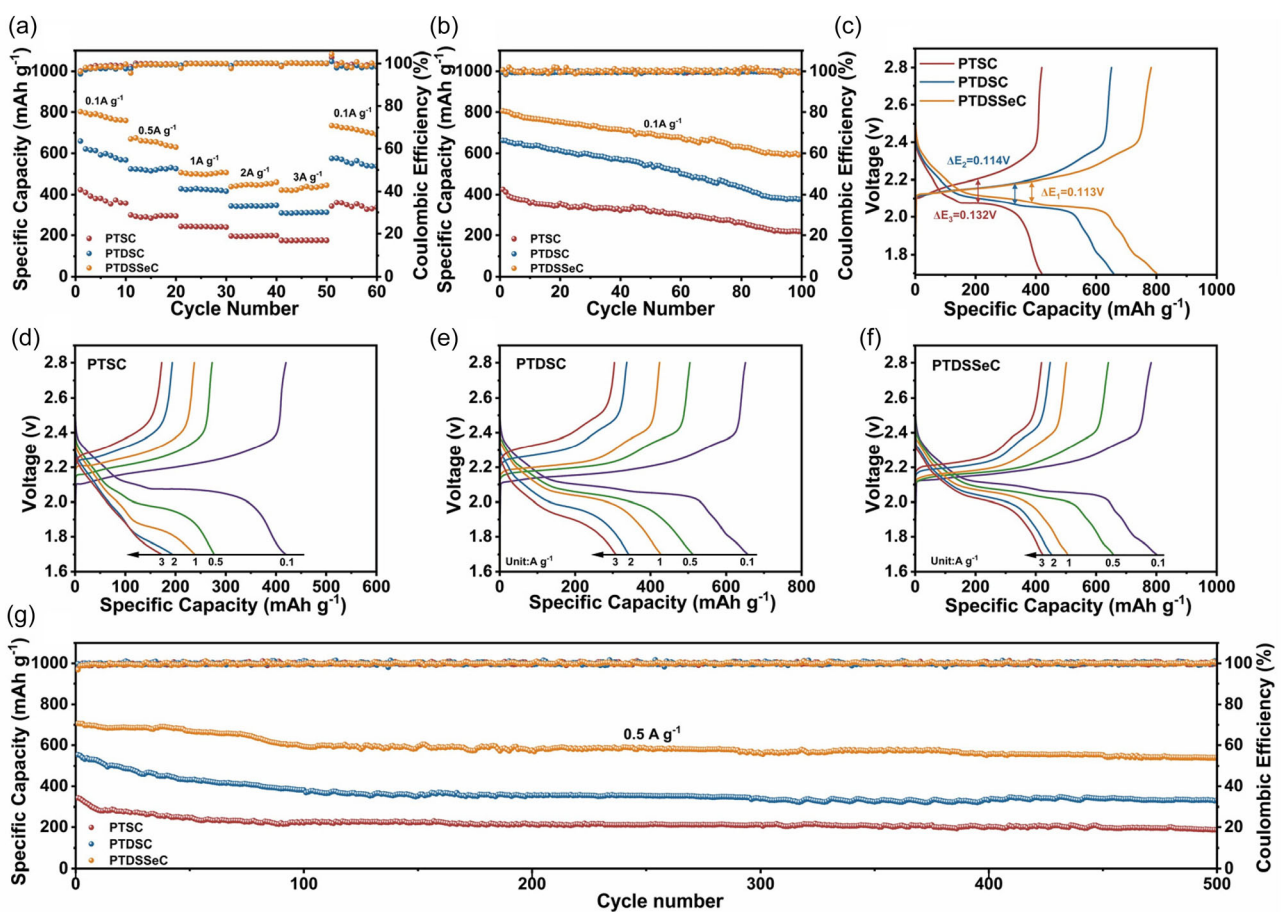


Figure 5. a) Rate performance, and b) cycling performance at 0.1 A g⁻¹ and c) GCD curves at 0.1 A g⁻¹ of PTSC, PTDSC, and PTDSSeC cathodes, respectively. GCD curves of d) PTSC, e) PTDSC, and f) PTDSSeC cathodes at different rates. g) Cycling performance at 0.5 A g⁻¹ of PTSC, PTDSC, and PTDSSeC cathodes, respectively.

retention rates of 54.3, 64.9, and 78.9%. As exhibited in Figure 5c, GCD curves of the three organic sulfur polymer cathodes at a current density of 0.1 A g^{-1} are provided, the charge/discharge plateau voltage difference (ΔE) of the PTDSSeC cathode is 0.113 V, which is lower than that of the PTSC cathode (0.132 V), this result suggests that the PTSC cathode requires overcoming a higher charge transfer barrier during charging and discharging process,^[57] which is consistent with the impedance performance of the polymer cathodes. Figure 5d-f shows the GCD of the PTSC, PTDS, and PTDSSeC cathodes at different rates, respectively. It can be seen that the GCD curves of three cathodes all exhibit single charge/discharge plateaus at different rates without showing the multiplateau characteristics of traditional S_8 cathodes, efficaciously proving that the designed short sulfur chains enables the sulfides in the cathode material to maintain a "solid-solid" reaction mechanism during charge/discharge,^[58] effectively inhibiting the shuttle effect. Among them, the PTDSSeC cathode has a smaller polarization phenomenon at different current densities, further proving the redox stability owing to codoping of pyridine groups and selenium atoms. Finally, 500-cycle long cycling detection is conducted at a current density of 0.5 A g^{-1} for the PTSC, PTDS, and PTDSSeC cathodes, respectively, as shown in Figure 5g. Initial specific capacities of three cathode materials are 343.2, 552.5, and $706.4 \text{ mA h g}^{-1}$, respectively, after 500 cycles the specific capacities are 185.3, 331.8, and $539.8 \text{ mA h g}^{-1}$, respectively, the capacity retention rates are 53.9, 60.1, and 76.4%, respectively, and the average Coulombic efficiency all exceeds 99%. Furthermore, areal capacity tests were conducted on PTSC, PTDS, and PTDSSeC cathodes at a current density of 0.663 mA cm^{-2} . As depicted in Figure S9, Supporting Information, the initial areal capacities of the three organosulfur cathode materials were 455.5, 733.2, and $937.3 \text{ mAh cm}^{-2}$, respectively, while after 500 cycles, the values were 245.9, 440.2, and $716.4 \text{ mAh cm}^{-2}$. Comprehensively, the above results prove that the organic sulfur cathode codoped with pyridine and selenium atoms exhibits higher capacity performance, better redox reversibility, and cycling stability due to its superior electron transport efficiency and redox kinetics properties.

3. Conclusions

In summary, this work proposes a synergistic strategy to improve battery capacity and cycle life through controlling short sulfur chains, pyridine groups, selenium atom doping, and CNT composite. Firstly, short sulfur chain (R—S4—R) covalently bonded to the propyl skeleton can effectively transform the cathode charge/discharge reaction from "solid–liquid–solid" dual plateau to "solid–solid" single plateau, fundamentally inhibiting the shuttle effect. Second, combined with the more conductive selenium atom reducing the charge transfer barrier, the pyridine ring with conjugated structure can speed up the electron transport velocity, significantly enhancing the ionic conductivity and conductivity of the organic sulfur cathode. Thirdly, the introduction of CNTs provides a fast electron transport channel for the organic sulfur cathode, further improving conductivity and spatially confining

polysulfides within the cathode. As a result, electrochemical analysis demonstrates that the PTDSSeC cathode doped with pyridine groups, selenium atoms, and CNTs exhibits excellent rate capability, and specific capacity of $706.4 \text{ mA h g}^{-1}$ at a current density of 0.5 A g^{-1} , possessing a capacity retention rate of 76.4% after 500 cycles, with an average coulombic efficiency exceeding 99.0%, meaningfully proving the superior reversible specific capacity and cycling durability. This strategy offers available insights via controlling the sulfur-chain length and introducing a functional group for fabricating high specific capacity and lifetime-stability lithium-organosulfur batteries.

Acknowledgements

This work was supported by the Project of National Natural Science Foundation (No. 52462034, 52262035), Major Science and Technology Project of Gansu Province (24ZD13GA018, 22ZD6GA008), Hongliu excellent youth project of Lanzhou University of technology and Key Research Program of Education Department of Gansu Province (GSSYLXM-03).

Conflict of Interest

The authors declare no conflict of interest.

Author Contributions

Wen-Wu Liu: funding acquisition (lead); project administration (lead); resources (lead); writing—review & editing (equal). **Hua-Xin Shen:** data curation (lead); methodology (lead); validation (lead); writing—original draft (lead). **Bo Lv:** formal analysis (lead); visualization (equal). **Ya-Wen Zheng:** conceptualization (equal); formal analysis (equal). **Rong Zou:** supervision (equal); validation (equal).

Data Availability Statement

The data that support the findings of this study are available from the corresponding author upon reasonable request.

Keywords: dual physical–chemical anchoring • organosulfur cathode • pyridine • selenium atomic doping • sulfur-chain length regulation

- [1] H. Song, K. Münch, X. Liu, K. Shen, R. Zhang, T. Weintraut, Y. Yusim, D. Jiang, X. Hong, J. Meng, Y. Liu, M. He, Y. Li, P. Henkel, T. Brezesinski, J. Janek, Q. Pang, *Nature* **2025**, 637, 846.
- [2] M. Liao, Y. Xu, M. M. Rahman, S. Tan, D. Wang, K. Wang, N. K. Dandu, Q. Lu, G. Li, L. Le, *Nat. Sustainability* **2024**, 7, 1709.
- [3] J. Li, L. Gao, F. Pan, C. Gong, L. Sun, H. Gao, J. Zhang, Y. Zhao, G. Wang, H. Liu, *Nano-Micro Lett.* **2024**, 16, 12.
- [4] Y. Chen, T. Wang, H. Tian, D. Su, Q. Zhang, G. Wang, *Adv. Mater.* **2021**, 33, 2003666.
- [5] A. D. Pathak, E. Cha, W. Choi, *Energy Storage Mater.* **2024**, 72, 103711.

- [6] J. Lee, C. Zhao, C. Wang, A. Chen, X. Sun, K. Amine, G.-L. Xu, *Chem. Soc. Rev.* **2024**, *53*, 5264.
- [7] Q. Liang, S. Wang, Y. Yao, P. Dong, H. Song, *Adv. Funct. Mater.* **2023**, *33*, 2300825.
- [8] S. Deng, T. Guo, J. Heier, C. Zhang, *Adv. Sci.* **2023**, *10*, 2204930.
- [9] S. F. Ng, M. Y. L. Lau, W. J. Ong, *Adv. Mater.* **2021**, *33*, 2008654.
- [10] D. Su, D. Zhou, C. Wang, G. Wang, *Adv. Funct. Mater.* **2018**, *28*, 1800154.
- [11] H. Li, S. Ma, J. Li, F. Liu, H. Zhou, Z. Huang, S. Jiao, Y. Kuang, *Energy Storage Mater.* **2020**, *26*, 203.
- [12] B. Li, Y. Chao, M. Li, Y. Xiao, R. Li, K. Yang, X. Cui, G. Xu, L. Li, C. Yang, *Electrochem. Energy Rev.* **2023**, *6*, 7.
- [13] H. Adenusi, G. A. Chass, S. Passerini, K. V. Tian, G. Chen, *Adv. Energy Mater.* **2023**, *13*, 2203307.
- [14] X. Yang, J. Luo, X. Sun, *Chem. Soc. Rev.* **2020**, *49*, 2140.
- [15] G. Li, J. Hu, G. Li, S. Ye, X. Gao, *J. Power Sources* **2013**, *240*, 598.
- [16] W. Ahn, K.-B. Kim, K.-N. Jung, K.-H. Shin, C.-S. Jin, *J. Power Sources* **2012**, *202*, 394.
- [17] R. Fang, S. Zhao, S. Pei, X. Qian, P.-X. Hou, H.-M. Cheng, C. Liu, F. Li, *ACS Nano* **2016**, *10*, 8676.
- [18] H. Shi, W. Lv, C. Zhang, D. W. Wang, G. Ling, Y. He, F. Kang, Q. H. Yang, *Adv. Funct. Mater.* **2018**, *28*, 1800508.
- [19] G. He, S. Evers, X. Liang, M. Cuisinier, A. Garsuch, L. F. Nazar, *ACS Nano* **2013**, *7*, 10920.
- [20] W. Tian, H. Zhang, X. Duan, H. Sun, G. Shao, S. Wang, *Adv. Funct. Mater.* **2020**, *30*, 1909265.
- [21] L. Chen, G. Cao, Y. Li, G. Zu, R. Duan, Y. Bai, K. Xue, Y. Fu, Y. Xu, J. Wang, *Nano-Micro Lett.* **2024**, *16*, 97.
- [22] J. Shen, X. Xu, J. Liu, Z. Liu, F. Li, R. Hu, J. Liu, X. Hou, Y. Feng, Y. Yu, *ACS Nano* **2019**, *13*, 8986.
- [23] J.-L. Yang, D.-Q. Cai, Q. Lin, X.-Y. Wang, Z.-Q. Fang, L. Huang, Z.-J. Wang, X.-G. Hao, S.-X. Zhao, J. Li, *Nano Energy* **2022**, *91*, 106669.
- [24] J. Xu, T. Lawson, H. Fan, D. Su, G. Wang, *Adv. Energy Mater.* **2018**, *8*, 1702607.
- [25] S. Bai, X. Liu, K. Zhu, S. Wu, H. Zhou, *Nat. Energy* **2016**, *1*, 1.
- [26] C. Lu, R. Fang, X. Chen, *Adv. Mater.* **2020**, *32*, 1906548.
- [27] Z. Zhang, L. Kong, S. Liu, G. R. Li, X. P. Gao, *Adv. Energy Mater.* **2017**, *7*, 1602543.
- [28] X. Wang, C. Yang, X. Xiong, G. Chen, M. Huang, J.-H. Wang, Y. Liu, M. Liu, K. Huang, *Energy Storage Mater.* **2019**, *16*, 344.
- [29] M. Cheng, R. Yan, Z. Yang, X. Tao, T. Ma, S. Cao, F. Ran, S. Li, W. Yang, C. Cheng, *Adv. Sci.* **2022**, *9*, 2102217.
- [30] P. Wang, D. Zhao, L. Yin, *Energy Environ. Sci.* **2021**, *14*, 1794.
- [31] Q. Zeng, R. Zhang, H. Lu, J. Yang, J. Rong, J. Weng, B. Zhang, S. Xiong, Q. Zhang, S. Huang, *Energy Environ. Sci.* **2025**, *18*, 1343.
- [32] R. Zou, W. Liu, F. Ran, *InfoMat* **2022**, *4*, e12319.
- [33] R. Fang, J. Xu, D.-W. Wang, *Energy Environ. Sci.* **2020**, *13*, 432.
- [34] P. Sang, Q. Chen, D.-Y. Wang, W. Guo, Y. Fu, *Chem. Rev.* **2023**, *123*, 1262.
- [35] X. Li, L. Yuan, D. Liu, J. Xiang, Z. Li, Y. Huang, *Small* **2022**, *18*, 2106970.
- [36] X. Yang, X. Li, K. Adair, H. Zhang, X. Sun, *Electrochim. Energy Rev.* **2018**, *1*, 239.
- [37] T. Wu, M. Jing, L. Yang, G. Zou, H. Hou, Y. Zhang, Y. Zhang, X. Cao, X. Ji, *Adv. Energy Mater.* **2019**, *9*, 1803478.
- [38] Y. Yang, G. Zheng, Y. Cui, *Chem. Soc. Rev.* **2013**, *42*, 3018.
- [39] S. Zhao, Y. Kang, M. Liu, B. Wen, Q. Fang, Y. Tang, S. He, X. Ma, M. Liu, Y. Yan, *J. Mater. Chem. A* **2021**, *9*, 18927.
- [40] R. Xiao, Z. Qu, J. Ren, G. Wang, Z. Sun, F. Li, *Adv. Energy Mater.* **2025**, *25*, 2501926.
- [41] D. Kong, W. Guo, Y. Zhao, Y. Zhao, *Adv. Energy Mater.* **2025**, *15*, 2403983.
- [42] Y.-W. Zheng, W.-W. Liu, H.-X. Shen, Y.-Z. Wu, F. Ran, *J. Colloid Interface Sci.* **2025**, *688*, 443.
- [43] L. Zhou, S. Jo, M. Park, L. Fang, K. Zhang, Y. Fan, Z. Hao, Y. M. Kang, *Adv. Energy Mater.* **2021**, *11*, 2003054.
- [44] E.-S. M. Duraia, A. Fahami, G. W. Beall, *J. Electron. Mater.* **2018**, *47*, 1176.
- [45] P. Sang, J. Song, W. Guo, Y. Fu, *Chem. Eng. J.* **2021**, *415*, 129043.
- [46] L. Xiao, Y. Cao, J. Xiao, B. Schwenzer, M. H. Engelhard, L. V. Saraf, Z. Nie, G. J. Exarhos, J. Liu, *J. Mater. Chem. A* **2013**, *1*, 9517.
- [47] J. Ruan, T. Yuan, Y. Pang, S. Luo, C. Peng, J. Yang, S. Zheng, *Carbon* **2018**, *126*, 9.
- [48] V. Krylova, N. Dukštinė, *Appl. Surf. Sci.* **2019**, *470*, 462.
- [49] J. Wu, Y. Lu, X. Ke, L. Zheng, R. Liao, D. Wu, *Natl. Sci. Rev.* **2025**, *12*, nwae421.
- [50] K. Ackermann, J. Koster, S. Schlücker, *Chem. Phys.* **2009**, *355*, 81.
- [51] Y. Cui, J. D. Ackerson, Y. Ma, A. Bhargav, J. A. Karty, W. Guo, L. Zhu, Y. J. A. f. m. Fu, *Adv. Funct. Mater.* **2018**, *28*, 1801791.
- [52] J. Zhou, T. Qian, N. Xu, M. Wang, X. Ni, X. Liu, X. Shen, C. Yan, *Adv. Mater.* **2017**, *29*, 1701294.
- [53] M. Zhao, H. J. Peng, J. Y. Wei, J. Q. Huang, B. Q. Li, H. Yuan, Q. Zhang, *Small Methods* **2020**, *4*, 1900344.
- [54] W. Weppner, R. A. Huggins, *J. Electrochem. Soc.* **1977**, *124*, 1569.
- [55] V. Kolosnitsyn, E. Kuzmina, E. Karaseva, S. Mochalov, *J. Power Sources* **2011**, *196*, 1478.
- [56] R. He, Y. Li, Z. Yin, H. Liu, Y. Jin, Y. Zhang, H. Liu, X. Zhang, *ACS Appl. Energy Mater.* **2023**, *6*, 3903.
- [57] E. T. Kim, J. Park, C. Kim, A. G. Simmonds, Y.-E. Sung, J. Pyun, K. Char, *ACS Macro Lett.* **2016**, *5*, 471.
- [58] W. P. Wang, J. Zhang, J. Chou, Y. X. Yin, Y. You, S. Xin, Y. G. Guo, *Adv. Energy Mater.* **2021**, *11*, 2000791.

Manuscript received: September 21, 2025

Revised manuscript received: October 20, 2025

Version of record online: